

TOWARD MORE REALISTIC ANALYTIC MODELS OF THE HELIOTAIL: INCORPORATING MAGNETIC FLATTENING VIA DISTORTION FLOWS

JENS KLEIMANN

Ruhr-Universität Bochum, Fakultät für Physik und Astronomie, Institut für Theoretische Physik IV, Bochum, Germany

CHRISTIAN RÖKEN

Universität Regensburg, Fakultät für Mathematik, Regensburg, Germany

HORST FICHTNER

Ruhr-Universität Bochum, Fakultät für Physik und Astronomie, Institut für Theoretische Physik IV, Bochum, Germany

JACOB HEERIKHUISEN

Department of Space Science and Center for Space Plasma and Aeronomic Research,
University of Alabama in Huntsville, Huntsville, AL 35899, USA

Draft version March 3, 2024

ABSTRACT

Both physical arguments and simulations of the global heliosphere indicate that the tailward heliopause is flattened considerably in the direction perpendicular to both the incoming flow and the large-scale interstellar magnetic field. Despite this fact, all of the existing global analytical models of the outer heliosheath's magnetic field assume a circular cross section of the heliotail. To eliminate this inconsistency, we introduce a mathematical procedure by which any analytically or numerically given magnetic field can be deformed in such a way that the cross sections along the heliotail axis attain freely prescribed, spatially dependent values for their total area and aspect ratio. The distorting transformation of this method honors both the solenoidality condition and the stationary induction equation with respect to an accompanying flow field, provided that both constraints were already satisfied for the original magnetic and flow fields prior to the transformation. In order to obtain realistic values for the above parameters, we present the first quantitative analysis of the heliotail's overall distortion as seen in state-of-the-art three-dimensional hybrid MHD–kinetic simulations.

Subject headings: ISM: magnetic fields — magnetohydrodynamics (MHD) – methods: analytical – Sun: heliosphere

1. INTRODUCTION

Our knowledge about the large-scale structure of the heliosphere has recently been increased significantly with the *Voyager 1* and *2* spacecraft that are by now exploring in situ the local interstellar medium (LISM; Gurnett et al. 2013) and the inner heliosheath (see, e.g. Richardson & Burlaga 2013), respectively. This progress is accompanied by insights gained from the remote measurements of energetic neutral atoms (ENAs) with the *Interstellar Boundary Explorer (IBEX)*; see the recent review by McComas et al. (2014). The *IBEX* observations supplement those made with the *Voyagers* particularly regarding the global structure of the heliosphere because they are not limited to its upwind hemisphere but comprise its entirety. While in this way the expected principal upwind–downwind asymmetry of the heliosphere could be confirmed, the actual structure of its downwind hemisphere is still under debate. However, there can be no doubt that the dominant feature of the downwind heliosphere is the so-called heliotail, along which

the solar wind (SW) plasma eventually merges into the LISM. Consequently, this heliotail — predicted to exist already by Parker (1961) — is a natural feature of all classical models describing the interaction of the SW with the LISM. Nonetheless, its detailed structure has been the subject of only a few studies. In an early paper, Yu (1974) analyzed the magnetized “wake” of the SW under the influence of charge exchange with interstellar hydrogen atoms. This line of research was continued only much later by Jäger & Fahr (1998) and Izmodenov & Alexashov (2003). While both papers confirmed the significance of this process, the latter authors discussed a length of the heliotail of several tens of thousands AU, whereas the former favored a value of not more than 1,500 AU. Additionally, Jäger & Fahr (1998) recognized the potential significance of the heliotail for the production of pick-up ions (PUIs). The related ENAs were studied by Czechowski & Grzedzielski (1998), who furthermore demonstrated how the direction and strength of an interstellar magnetic field (ISMF) can be deduced from the direction of the heliotail, an idea that was recently revived by McComas et al. (2013). Quantitative models of the form and deflection of the heliotail in the presence of a magnetized LISM were first presented by Ba-

naszkievicz & Ratkiewicz (1989), Matsuda & Fujimoto (1993), and Pogorelov & Matsuda (1998). Ratkiewicz et al. (2000), while not explicitly addressing the heliotail topic, provided a classification of the asymmetries and distortions resulting from different ISMF orientations and mentioned a flattening effect, which is also of relevance for the heliotail. Very recent studies looked at the stability of the heliotail (Pogorelov et al. 2014, 2015) and at the idea of its “splitting” (Drake et al. 2015; Opher et al. 2015), and, thereby, revived work on two topics that were also discussed to some extent already by Yu (1974).

The heliotail is not only of significance for the flux of PUIs and ENAs but also for that of cosmic rays (CRs). At the end of the last century, a so-called heliomagnetotail anisotropy in the CR flux in the low-TeV range was discovered by Nagashima et al. (1998). This dipole-structured anisotropy and its — at least approximate — relation to the heliotail was confirmed by the latest generation of large-area detectors like MILAGRO, the Tibet Air Shower, IceCube, and others (Guilian et al. 2007; Amenomori & Tibet As γ Collaboration 2010; Karapetyan 2010; Grigat & Pierre AUGER Collaboration 2011), showing an enhancement in the permille range of the low-TeV particle flux in the direction of the heliotail. A temporary denial of a physical link between the heliotail and this anisotropy was based on the facts (i) that the density in a gravitationally focused tail of interstellar material would be much too low to explain the signal in terms of secondary neutron production (Drury & Aharonian 2008), and (ii) that the gyro-radii of particles at 10 TeV are about equal to the size of the heliosphere or greater (Abbasi et al. 2010). Recently, however, Lazarian & Desiati (2010) have proposed a new physical link between the tail and the CR anisotropy by invoking magnetic reconnection as a process that accelerates CRs in the 50 GeV to 10 TeV range in the heliotail. While the existence of such a local source of CRs might be doubtful, in a subsequent paper, Desiati & Lazarian (2013) considered the more likely anisotropy-inducing effect of the ISMF, whose homogeneity on the scale of the heliosphere is disturbed by the presence of the latter (see Röken et al. 2015, and references therein). They claim that the large-scale CR anisotropy below 100 TeV is mostly shaped by particle interactions with turbulent ripples generated by the interaction of the heliospheric and the interstellar magnetic fields.

None of these explanations or first “exploratory” modeling attempts were based on sophisticated heliospheric or advanced CR transport models, which are, however, both necessary in order to derive quantitative results that can be compared to observations. This gap has recently been filled with the work by Schwadron et al. (2014) and Zhang et al. (2014), who studied the problem in much more detail by particularly computing CR trajectories (as was first done by Washimi et al. 1999) rather than by employing the CR diffusion approximation, which would represent a conceptual extreme in that case. These two papers arrived at the conclusion that a heliospheric impact on the CR anisotropy up to the TeV range must indeed be expected. Both studies, however, still have their drawbacks: Either an analytical model that is probably too simplifying (Schwadron et al. 2014), or a numerical input, which is difficult to handle (Zhang et al. 2014), is used for the local ISMF configuration.

For further analysis of the CR anisotropy problem, it is therefore desirable to have a significantly improved analytical model that incorporates crucial features of the ISMF.

A first step to construct such a model was made by Röken et al. (2015), who derived an exact analytical solution for the local ISMF assumed to be frozen into the interstellar plasma flow. Not only this but, to the best of our knowledge, all other analytical models of the local ISMF (Whang 2010; Schwadron et al. 2014; Isenberg et al. 2015) feature a circular cross section of the heliotail, i.e. far downtail, the heliopause takes the shape of a semi-infinite cylinder. Nonetheless, the *IBEX* measurements (McComas et al. 2013) as well as several numerical studies (e.g. Heerikhuisen et al. 2014; Wood et al. 2014) have confirmed the intuitive notion that with growing heliocentric distance, the heliotail becomes increasingly compressed perpendicular to the directions of the undisturbed ISMF and the incoming interstellar flow. Therefore, we propose a method by which both the magnetic field \mathbf{B} and a possibly associated flow field \mathbf{u} , or in fact any other such vector field, may be deformed in a well-defined manner into a realistic configuration, such that it is still maintaining both the field line topology and the basic condition that the solenoidal magnetic field is frozen into the (possibly, but not necessarily equally solenoidal) plasma flow. In other words, if

$$\nabla \cdot \mathbf{B} = 0 \quad (1)$$

and

$$\nabla \times (\mathbf{u} \times \mathbf{B}) = \mathbf{0} \quad (2)$$

were satisfied by the model’s initial fields, then they will continue to be satisfied by the deformed vector fields.

The outline of the paper is as follows. In Section 2, the mathematical concept of distortion flows for the deformation of vector fields is introduced and the equations relevant for the procedure are derived. Section 3 provides some guidance for the choice of realistic parameters by extracting the relevant data from self-consistent global simulations of the heliosphere, and applies them to the Röken et al. (2015) model. Finally, Section 4 completes the paper with a summary and conclusions. The fact that our method honors both the magnetic solenoidality condition (1) and the stationary induction equation (2) is proven rigorously in Appendix A, while Appendices B and C provide some details on the general distortion transformation and the employed data fitting method, respectively.

2. DERIVATION OF THE DISTORTION FLOW METHOD

In order to deform a given pair of magnetic and velocity fields, we introduce the auxiliary field, \mathbf{w}_0 , in which these fields are advected. The geometrical shapes of the distorted fields can be controlled by choosing a suitable form of \mathbf{w}_0 .

2.1. The Case of Constant Cross-sectional Areas

In view of the intended application to the heliotail, we want to contract the initially circular cross-section in one direction and expand it in the perpendicular direction.

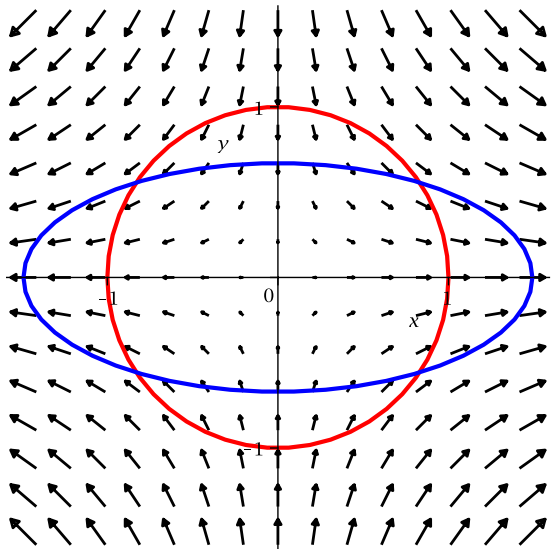


Figure 1. The flow field (3), together with an initially circular set of points at time $t = 0$ (red) and the advected points at later time $t = t_1 = 0.2/\alpha > 0$ (blue), when the distortion has reached an aspect ratio of $\eta = \exp(0.4) \approx 1.49$ according to Eq. (7).

To this end, we first consider the two-dimensional (2D) velocity field

$$\mathbf{w}_0 : \mathbb{R}^2 \rightarrow \mathbb{R}^2, \quad \begin{pmatrix} x \\ y \end{pmatrix} \mapsto \begin{pmatrix} \alpha x \\ -\alpha y \end{pmatrix} \quad (3)$$

with constant $\alpha > 0$. The equation of motion for an inertialess particle being passively advected in this flow is

$$\dot{\mathbf{r}}(t) = \mathbf{w}_0[\mathbf{r}(t)], \quad (4)$$

the solution of which, subjected to the initial condition $\mathbf{r}(0) = \mathbf{r}_0$, reads

$$\begin{pmatrix} x(t) \\ y(t) \end{pmatrix} = \begin{pmatrix} x_0 \exp(\alpha t) \\ y_0 \exp(-\alpha t) \end{pmatrix}. \quad (5)$$

Specifically, an ensemble of particles which at $t = 0$ forms a unit circle will at $t = t_1 \geq 0$ have been deformed into an ellipse of half-axes

$$(a, b) := (\exp(\alpha t_1), \exp(-\alpha t_1)) \quad (6)$$

with aspect ratio

$$\eta := \frac{a}{b} = \exp(2\alpha t_1) \geq 1 \quad (7)$$

while maintaining its area ($\propto ab = 1$), in agreement with $\nabla \cdot \mathbf{w}_0 = 0$ (see Fig. 1).

The idea is now to prescribe for each position z along the heliotail axis a “target aspect ratio” $\eta(z) = a(z)/b(z)$ into which the initially circular cross sections are to be deformed by an embedding of (5) into three-dimensional (3D) space

$$x(t_1) = x_0 \exp[+\alpha(z_0) t_1] \quad (8)$$

$$y(t_1) = y_0 \exp[-\alpha(z_0) t_1] \quad (9)$$

$$z(t_1) = z_0 \quad (10)$$

as the solution to Eq. (4), evaluated at a fixed $t = t_1$. This motivates a mapping $\mathbb{R}^3 \rightarrow \mathbb{R}^3$

$$x = a(z) x_0 \quad (11)$$

$$y = b(z) y_0 \quad (12)$$

$$z = z_0 \quad (13)$$

from arbitrary undeformed coordinates $\mathbf{r}_0 = (x_0, y_0, z_0)$ at $t = 0$ to deformed coordinates $\mathbf{r} = (x, y, z)$ at $t = t_1$, where $a(z)$ and $b(z)$ are given by Eq. (6) with $\alpha = \alpha(z)$. Note that this deformation has to be understood in the sense of a discrete transformation $t = 0 \rightarrow t_1$, in contrast to the t -dependent, continuous case (cf. Section 2.3). Moreover, the requirement to ensure the constancy of the cross-sectional area $\pi a(z)b(z)$ for any z implies

$$a(z) = \eta(z)^{1/2} \quad \text{and} \quad b(z) = \eta(z)^{-1/2}. \quad (14)$$

To see how a deformed vector $\mathbf{P} \in \{\mathbf{u}, \mathbf{B}\}$ is obtained via the distortion field \mathbf{w}_0 , consider the unsqueezed vector \mathbf{P}_0 located at \mathbf{r}_0 and pointing in the direction of $\delta\mathbf{r}_0$, i.e. $\mathbf{P}_0 = \nu \delta\mathbf{r}_0$, where $\delta\mathbf{r}_0$ is a small displacement vector, which may also be pictured as a small segment of a field line. The constant ν is introduced to warrant dimensional consistency, and can be used to accommodate scalings of a desired magnitude. Via Eq. (11), the x component of the deformed vector \mathbf{P} at its new position \mathbf{r} becomes

$$\begin{aligned} P_x(\mathbf{r}) &= \nu [(x + \delta x) - x] \\ &= \nu [a(z + \delta z) (x_0 + \delta x_0) - a(z) x_0] \\ &\approx \nu [a(z) \delta x_0 + a'(z) x_0 \delta z] \\ &= a(z) P_{0x}(\mathbf{r}_0) + a'(z) x_0 P_{0z}(\mathbf{r}_0), \end{aligned} \quad (15)$$

where a prime denotes differentiation with respect to z , and the “ \approx ” symbol has been used only because the terms of $\mathcal{O}(\delta^2)$ have been neglected in the Taylor expansion of $a(z + \delta z)$. The y component is found in complete analogy, and since the z component remains unaffected (i.e. $z_0 = z$), we end up with

$$\begin{pmatrix} P_x \\ P_y \\ P_z \end{pmatrix} = \begin{pmatrix} a P_{0x} \\ b P_{0y} \\ 0 \end{pmatrix} + P_{0z} \begin{pmatrix} (a'/a) x \\ (b'/b) y \\ 1 \end{pmatrix}. \quad (16)$$

In other words, given an arbitrary, unsqueezed vector field \mathbf{P}_0 , together with the function $\eta(z)$ specifying the desired aspect ratio relative to a circle, the components of the distorted field \mathbf{P} at position \mathbf{r} can be obtained by

1. finding the corresponding “starting location” $\mathbf{r}_0(\mathbf{r}) = (x/a(z), y/b(z), z)$;
2. evaluating $\mathbf{P}_0(\mathbf{r}_0)$ at this position; and
3. transforming the result according to Eq. (16).

For scalar quantities Q such as mass density or temperature, which contain no directional information, the proper form after distortion is simply $Q(\mathbf{r}) = Q_0(\mathbf{r}_0)$.

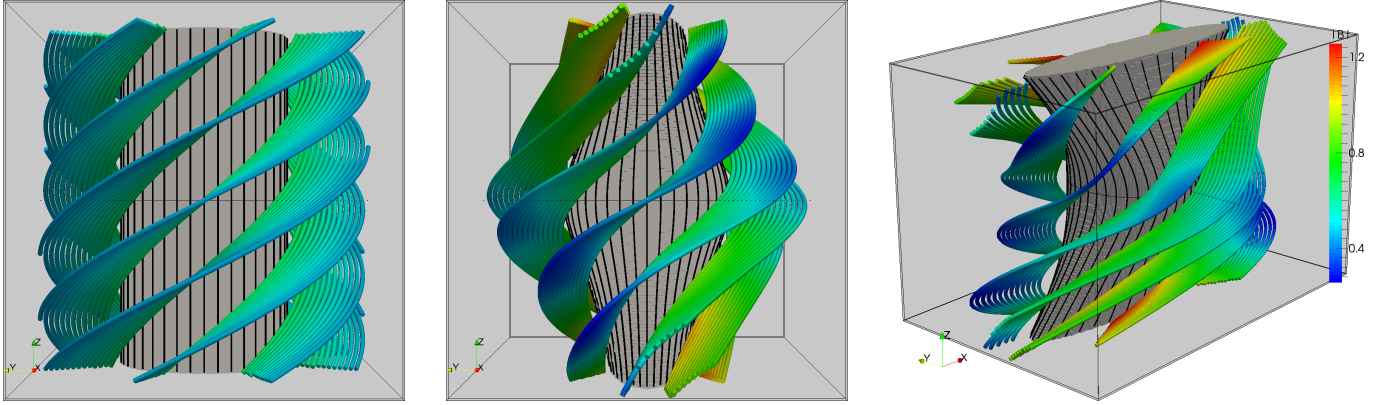


Figure 2. Left: selected field lines of the undistorted flux tube (17). Middle: the corresponding magnetic field lines (24) after a distortion according to Eqs. (19)–(20) has been applied, viewed along the major (x) axis. Right: the same situation viewed from a different angle. The gray surface indicates the cylinder $\rho^2 = x^2 + y^2 = 1$ (left), which is transformed into the shape $[x/a(z)]^2 + [y/b(z)]^2 = 1$ via the squeezing transformation (16).

In the above derivation, the distortion flow \mathbf{w}_0 (which mediates the deformation) is an auxiliary field that must be carefully distinguished from the actual velocity field \mathbf{u} upon which the transformation acts. \mathbf{w}_0 is thus simply a mathematical object that acts similar to a flow field, although no physical flow of matter is associated with it. Likewise, the parameter t , which we have referred to as “time” for the sake of clarity, is rather to be understood as a deformation parameter controlling the extent of deformation from the original field $\mathbf{P}_0 \in \{\mathbf{u}_0, \mathbf{B}_0\}$ (at “time” $t = 0$) to its distorted counterpart $\mathbf{P} \in \{\mathbf{u}, \mathbf{B}\}$ at $t = t_1$. We continue to use the symbol t since the stationary induction equation (2) implies that the configuration formed by \mathbf{u} and \mathbf{B} does not depend on physical time, such that no confusion should arise from this terminology.

2.2. A Simple Example

To illustrate the procedure, consider the cylindrical magnetic flux tube

$$\begin{aligned} \mathbf{B}_0(\mathbf{r}_0) &= \frac{\rho_0}{1 + \rho_0^2} \mathbf{e}_{\varphi_0} + \frac{1}{1 + \rho_0^2} \mathbf{e}_{z_0} \\ &= \frac{1}{1 + x_0^2 + y_0^2} \begin{pmatrix} -y_0 \\ x_0 \\ 1 \end{pmatrix} \end{aligned} \quad (17)$$

(where $\rho_0 := \sqrt{x_0^2 + y_0^2}$ denotes the cylindrical radial coordinate and $\varphi_0 := \arctan(y_0/x_0)$ the corresponding angular coordinate), together with a helical “swirl flow”

$$\mathbf{u}_0(\mathbf{r}_0) = \Omega \rho_0 \mathbf{e}_{\varphi_0} + V \mathbf{e}_{z_0} = \begin{pmatrix} -\Omega y_0 \\ \Omega x_0 \\ V \end{pmatrix}, \quad (18)$$

characterized by constants $\Omega, V \in \mathbb{R}$. It can easily be shown that these fields satisfy both $\nabla_0 \times (\mathbf{u}_0 \times \mathbf{B}_0) = \mathbf{0}$ and $\nabla_0 \cdot \mathbf{B}_0 = 0$. In this example, we choose a deformation with a spatially variable aspect ratio $\eta(z) = 1 + z^2$,

which implies

$$a(z) = \sqrt{1 + z^2} \quad (19)$$

$$b(z) = \frac{1}{\sqrt{1 + z^2}} \quad (20)$$

according to Eq. (14). Since we are interested in the explicit forms of the distorted fields \mathbf{B} and \mathbf{u} , we now express all points (x_0, y_0, z_0) in $\mathbf{P}_0(\mathbf{r}_0)$ through (x, y, z) and apply the transformation (16) to the fields (17) and (18). Thus, with

$$\begin{aligned} P_x(x, y, z) &= a(z) P_{0x} \left(\frac{x}{a(z)}, \frac{y}{b(z)}, z \right) \\ &\quad + \frac{a'(z)}{a(z)} x P_{0z} \left(\frac{x}{a(z)}, \frac{y}{b(z)}, z \right) \end{aligned} \quad (21)$$

$$\begin{aligned} P_y(x, y, z) &= b(z) P_{0y} \left(\frac{x}{a(z)}, \frac{y}{b(z)}, z \right) \\ &\quad + \frac{b'(z)}{b(z)} y P_{0z} \left(\frac{x}{a(z)}, \frac{y}{b(z)}, z \right) \end{aligned} \quad (22)$$

$$P_z(x, y, z) = P_{0z} \left(\frac{x}{a(z)}, \frac{y}{b(z)}, z \right), \quad (23)$$

we obtain the distorted fields

$$\begin{aligned} \mathbf{B} &= \frac{1}{1 + x^2 + y^2(1 + z^2)^2 + z^2} \\ &\quad \times \begin{pmatrix} xz - y(1 + z^2)^2 \\ x - yz \\ 1 + z^2 \end{pmatrix} \end{aligned} \quad (24)$$

$$\mathbf{u} = \frac{1}{1 + z^2} \begin{pmatrix} xzV - y(1 + z^2)^2\Omega \\ x\Omega - yzV \\ (1 + z^2)V \end{pmatrix}, \quad (25)$$

which can again be verified to satisfy the desired constraints (1) and (2). Fig. 2 illustrates the magnetic field configuration before and after the deformation.

2.3. Relation to Inductive Flux Transport

The advection of field lines via distortion flows is reminiscent of the transport of frozen-in field lines via the classical induction equation of ideal MHD (e.g. Childress & Gilbert 1995). It is therefore reasonable to ask how the method detailed above relates to physical flux transport via an induction-type equation

$$\partial_t \mathbf{P} = \nabla \times (\mathbf{w} \times \mathbf{P}) \quad (26)$$

that would lead to a similar result, however, for continuous deformations with respect to t described by the transformation $(\mathbf{r}_0, t) \mapsto (\mathbf{r}(\mathbf{r}_0, t), t)$. To clarify this point, we first derive the explicit evolution equation that is actually solved by the fields given by the distortion flow method. In the spirit of Eq. (15), but now with a varying time/deformation parameter t , the vector field $\mathbf{P}(\mathbf{r}, t)$ at position $\mathbf{r} = \mathbf{r}(\mathbf{r}_0, t)$ and consecutive times t and $t + \delta t$ is

$$\mathbf{P}(\mathbf{r}, t) = \nu [\hat{\mathbf{r}}(\mathbf{r}, t) - \mathbf{r}(\mathbf{r}_0, t)] = \nu \delta \mathbf{L}(\mathbf{r}, t) \quad (27)$$

$$\begin{aligned} \mathbf{P}(\mathbf{r}, t + \delta t) &= \nu [\hat{\mathbf{r}}(\mathbf{r}, t + \delta t) - \mathbf{r}(\mathbf{r}_0, t + \delta t)] \quad (28) \\ &= \nu \delta \mathbf{L}(\mathbf{r}, t + \delta t), \end{aligned}$$

where $\delta \mathbf{L}$ denotes a small, time-dependent displacement vector, and $\hat{\mathbf{r}} := \mathbf{r} + \delta \mathbf{L}$. Note that $t \mapsto \mathbf{r}(\mathbf{r}_0, t)$ is the trajectory starting at \mathbf{r}_0 , along which the \mathbf{P} vector moves due to the action of the distortion flow \mathbf{w} , yielding evolutionary deformation. Expanding (28) for small δt , subtracting (27), and neglecting the terms of $\mathcal{O}(\delta t^2)$, we obtain

$$\begin{aligned} \left(\frac{d\mathbf{r}}{dt} \cdot \nabla \right) \mathbf{P} + \partial_t \mathbf{P} &= \nu \left(\frac{d\hat{\mathbf{r}}}{dt} - \frac{d\mathbf{r}}{dt} \right) \\ &= \nu [\mathbf{w}(\mathbf{r} + \delta \mathbf{L}) - \mathbf{w}(\mathbf{r})] \quad (29) \\ &\approx \nu (\delta \mathbf{L} \cdot \nabla) \mathbf{w}(\mathbf{r}), \end{aligned}$$

where the evolution equation

$$\frac{d\mathbf{r}}{dt} = \mathbf{w}(\mathbf{r}) \quad (30)$$

and a Taylor expansion of $\mathbf{w}(\mathbf{r} + \delta \mathbf{L})$ for small $\delta \mathbf{L}$ up to first order have been used. Substituting Eq. (27) and again (30) into (29), one finds

$$\begin{aligned} \partial_t \mathbf{P} &= (\mathbf{P} \cdot \nabla) \mathbf{w} - (\mathbf{w} \cdot \nabla) \mathbf{P} \\ &= \nabla \times (\mathbf{w} \times \mathbf{P}) - (\nabla \cdot \mathbf{P}) \mathbf{w} + (\nabla \cdot \mathbf{w}) \mathbf{P}, \quad (31) \end{aligned}$$

which shows explicitly that the distortion flow method becomes equivalent to solving the ‘‘induction equation’’ (26) for the special case in which both $\nabla \cdot \mathbf{w}$ and $\nabla \cdot \mathbf{P}$ vanish. So in principle, one could as well use (26) to obtain some form of distorted fields, in which case $\partial_t (\nabla \cdot \mathbf{P}) = 0$ would even be satisfied unconditionally, i.e. without requiring any constraints on the value of $\nabla \cdot \mathbf{w}$. However, as can be shown using an analysis similar to the one presented toward the concluding part of Appendix A, the alternative evolution equation (26) can maintain $\nabla \times (\mathbf{u} \times \mathbf{B}) = \mathbf{0}$ only for the special case $\nabla \cdot \mathbf{P} = 0 = \nabla \cdot \mathbf{w}$, in which it becomes identical to Eq. (31) anyway. Additionally, analytical solutions to (26) are usually difficult to obtain even for simple choices of \mathbf{w} , whereas for the method proposed here, it suffices to solve the equation of motion (30), which will

be much simpler to do in most cases.

2.4. Generalization to Varying Cross-sectional Areas

For a given application, the condition that cross sections can change their shapes but not their absolute areas may not always be satisfied. (This certainly holds true in the case of the heliospheric tail, as will be shown in Section 3.2.) Therefore, we now wish to relax this constraint, such that $a(z)$ and $b(z)$ may be chosen independently of one another. Guided by our findings from the simpler situation considered so far, we will again take the distortion to be incompressible. This implies that the latter will no longer be confined to separate x - y planes, but that material from one z layer may be displaced into adjacent layers, i.e. the distortion flow corresponding to that of Eq. (3) will attain a non-zero z component.

So consider $a(z)$ and $b(z)$ as given independently of one another. In an incompressible distortion, the spatial volume element is to be conserved, i.e.

$$dx_0 dy_0 dz_0 = dx dy dz. \quad (32)$$

Additionally, we now allow for a prescribed displacement $m(z)$ along the x axis as a third free parameter besides $a(z)$ and $b(z)$. The x and y components of the transformation thus become

$$x_0 = \frac{x - m(z)}{a(z)} \quad \text{and} \quad y_0 = \frac{y}{b(z)}. \quad (33)$$

A similar displacement in the y direction could easily be accounted for as well. We will refrain from doing so for simplicity of argument, and also because it will not be relevant for the intended application to the heliotail (see Section 3). While various choices of $z_0 = z_0(x, y, z)$ would be consistent with Eq. (32), we restrict ourselves to the special case of $z_0 = z_0(z)$, describing the situation that all particles from the plane at z_0 are being shifted into another plane at z . The general case of $z_0 = z_0(x, y, z)$ is addressed in Appendix B. Consequently, the z component of the distortion transformation has to satisfy the relation

$$z_0 = \int_0^{z_0} d\tilde{z} \stackrel{!}{=} \int_0^z a(\tilde{z}) b(\tilde{z}) d\tilde{z} =: F(z) \quad (34)$$

in order to remain consistent with Eq. (32). As can be seen in this equation, $z = 0$ is to be interpreted as the ‘‘reference height’’ at which the transformation induces no vertical displacement of \mathbf{P} , i.e. the planes $z_0 = 0$ and $z = 0$ coincide.

Repeating the derivation of Eq. (15), we are led to

$$\begin{aligned} P_x(\mathbf{r}) &= \nu [(x + \delta x) - x] \\ &= \nu [a(z + \delta z) (x_0 + \delta x_0) + m(z + \delta z) \\ &\quad - a(z) x_0 - m(z)] \quad (35) \\ &\approx \nu [a(z) \delta x_0 + a'(z) \delta z x_0 + m'(z) \delta z] \\ &= a(z) P_{0x} + [a'(z) x_0 + m'(z)] P_z. \end{aligned}$$

The corresponding equation for P_y is found in complete analogy, except that both $m(z)$ and $m'(z)$ are absent. Introducing now $z = K(z_0)$ as the inverse of $z_0 = F(z)$,

we obtain

$$\begin{aligned}
 P_z(\mathbf{r}) &= \nu [(z + \delta z) - z] \\
 &= \nu [K(z_0 + \delta z_0) - K(z_0)] \\
 &= \nu [\partial_{z_0} K(z_0) \delta z_0 + \mathcal{O}(\delta z^2)] \\
 &\approx [a(z) b(z)]^{-1} P_{0z}
 \end{aligned} \tag{36}$$

for the z component. Inserting (36) into (35) and suppressing the argument z in a , b , and m , the complete vector transformation becomes

$$\begin{pmatrix} P_x \\ P_y \\ P_z \end{pmatrix} = \begin{pmatrix} a P_{0x} \\ b P_{0y} \\ 0 \end{pmatrix} + \frac{P_{0z}}{ab} \begin{pmatrix} a' x_0 + m' \\ b' y_0 \\ 1 \end{pmatrix}. \tag{37}$$

While in this form it looks very similar to its analog (16), the most important difference is hidden in the additional requirement to obtain z_0 as a function of z , which involves the evaluation of the integral (34). This procedure will be illustrated in Section 3.2.

3. REALISTIC PARAMETERS FOR THE HELIOTAIL

Returning to our intended application, the heliotail, the above considerations naturally provoke the question of how the z profiles for the squeezing functions a , b and the displacement m should be chosen in order to obtain a configuration that resembles actual heliospheric conditions as closely as possible.

3.1. Data Source and Fitting Method

To provide some guidance for these choices, we turn to the 3D plasma-neutral simulations of the interaction between the SW and the LISM performed by Heerikhuisen et al. (2014). These simulations employ an MHD solver (Pogorelov et al. 2006) for the ionized plasma and a Monte-Carlo particle-based Boltzmann solver (Heerikhuisen et al. 2006) for neutral hydrogen. The neutral component is coupled to the plasma through charge-exchange collisions that generate energy and momentum source terms which are applied to the MHD equations (Heerikhuisen & Pogorelov 2010). For the simulations considered here, the ion and neutral components were iterated until a steady-state solution to the SW-LISM boundary value problem was obtained. An important aspect of these simulations is the removal of energy from the SW through charge exchange with cold LISM hydrogen atoms as it flows down the heliotail. This leads to a reduction in pressure, and hence a decrease in the heliotail cross section at large distances. The simulations were performed on a spherical grid where the polar axis is aligned with the solar rotation axis, using an angular resolution of 3° in azimuth, 1.5° in colatitude, and a non-uniform radial grid with 284 cells. The inner boundary is located at 10 AU, and the outer boundary at 1,000 AU. The resulting heliotail extends well beyond the outer boundary in the downstream LISM direction. The cell size increases with radial distance, which can make it difficult to accurately determine the heliopause location in the distant heliotail. However, the bulk properties of the plasma and neutral populations and the overall shape of the heliosphere are not significantly affected by this reduction in resolution near the outer boundary.

Since these simulations were performed for magnetic field strengths of $B_{\text{isim}} \in \{1, 2, 3, 4\} \times 0.1$ nT, they resulted in four distinct 3D configurations after a steady state had been reached. Here, these four datasets were then subjected to the following analysis: For all combinations j of magnetic field strengths B_{isim} and chosen x - y coordinate planes with $z \in \{-100, -200, \dots, -800\}$ AU, the heliopause locations \mathcal{H}_j were determined as the isocontours in the x - y plane at which the plasma temperature has increased by a factor of five over its undisturbed LISM value at the outer computational boundary (see Fig. 6 in Heerikhuisen et al. 2014). Each \mathcal{H}_j is then typically given by $N \approx 200$ pairs of coordinates $(x_i, y_i)_j$, $i = 1, \dots, N$, which have been rotated around the inflow (z) axis such that the x direction coincides with the direction of \mathbf{B}_{isim} at infinity when projected onto the x - y plane. An ellipse

$$\mathcal{E}_j : \left(\frac{x_i - m_j}{a_j} \right)^2 + \left(\frac{y_i - m_{\perp,j}}{b_j} \right)^2 = 1 \tag{38}$$

(in which the second index j of x_i and y_i has been suppressed), with major semi-axis a_j , minor semi-axis b_j , and center coordinates $(m_j, m_{\perp,j})$ was then fitted to each \mathcal{H}_j contour by varying these four parameters until the total “difference area” Δ_j (i.e. the area covered by the interiors of either \mathcal{H}_j or \mathcal{E}_j , but not both) attained its global minimum. The explicit form of Δ_j is given in Appendix C. Here a_j , b_j , and m_j play the same role as the functions a , b , and m in the above derivation, except that they are no longer dimensionless but measured in absolute units of AU. Note that in order to obtain sufficiently good fitting results, we found it necessary also to allow for a displacement $m_{\perp,j}$ in the direction of \mathcal{E}_j ’s minor axis as a fourth parameter.

To illustrate this process, Fig. 3 shows the fitting results for the case of $z = -500$ AU, which was also used

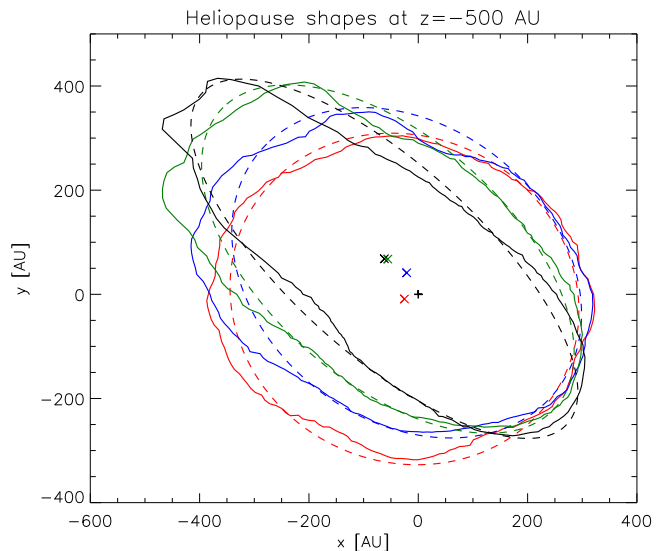


Figure 3. Heliopause contours at $z = -500$ AU as derived from the hybrid simulation for B_{isim} values of 0.1 (red), 0.2 (blue), 0.3 (green), and 0.4 nT (black), together with the respective fitting ellipses (dashed). The “+” symbol marks the inflow axis ($x = 0 = y$), while the “x” symbols indicate the centers of the respective ellipses.

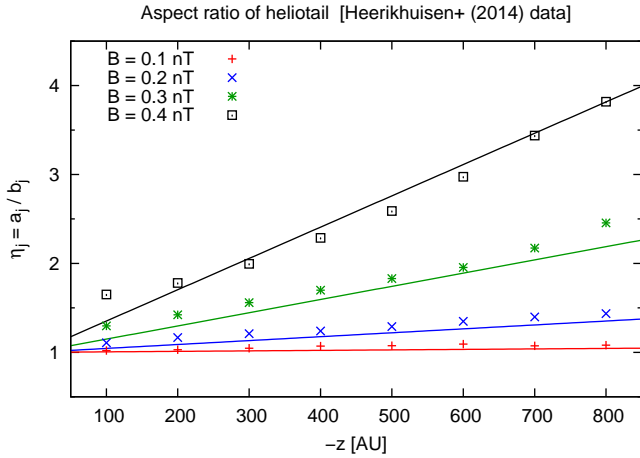


Figure 4. Aspect ratios η_j of fitting ellipses, together with fitting function (39).

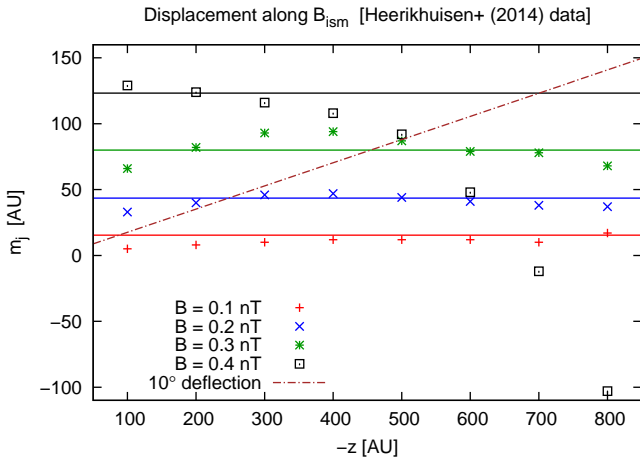


Figure 5. Linear displacement of the heliotail core axis against the inflow direction, together with fitting function (40). The dashed line marks a hypothetical deflection of 10° against the inflow axis. For the $B = 0.4$ nT case, data points at $z < -400$ AU were disregarded when setting up the fitting relation (40). This is justified by the observation that for these cases the heliopause contours develop a pronounced pear-shaped asymmetry that renders the elliptic approximation questionable.

for Fig. 6 in Heerikhuisen et al. (2014). The minus sign honors the convention that the LISM flow is incident from $z \rightarrow +\infty$, which will be exploited in Section 3.3. The parameters $\eta_j := a_j/b_j$ and m_j thus derived are displayed as functions of z in Figs. 4 and 5 along with the heuristic fitting functions

$$\eta_{\text{fit}}(B_{\text{ism}}, z) := 1 + 3.27 \left(\frac{-z}{100 \text{ AU}} \right) \left(\frac{B_{\text{ism}}}{\text{nT}} \right)^{2.5} \quad (39)$$

$$m_{\text{fit}}(B_{\text{ism}}, z) := (487 \text{ AU}) \left(\frac{B_{\text{ism}}}{\text{nT}} \right)^{1.5}, \quad (40)$$

which we propose to use as “best guesses” when setting up the deformation for a heliospheric field model. To our knowledge, this is the first time that simulations have been used to quantify the magnetic field-induced flattening and deflection of the heliotail.

While the cross-sectional flattening shows the expected behavior, i.e. it increases with both B_{ism} and distance $-z$, the fact that the derived displacement does not depend monotonously on z is somewhat at odds with the notion of the heliotail axis being deflected by a fixed angle against the inflow axis (which would imply $m_{\text{fit}} \sim z$ for fixed B_{ism}). At this point, we may only note that while the simulations at hand do not support a corresponding scaling relation, the absolute magnitude of deflection is indeed rather small, in agreement with Wood et al. (2014), who present observational constraints to argue for a deflection angle of the order of 10° and certainly below 20° .

The resulting distribution of $m_{\perp, \text{fit}}(B_{\text{ism}}, z)$ of absolute size (11 ± 6) AU and zero mean did not show any discernible systematics, and is therefore most likely due to the probabilistic nature of the hybrid MHD-kinetic approach (which can only accommodate a finite number of computational particles for the neutral component). Besides this, the only other cause for a departure of the problem’s symmetry with respect to the $\mathbf{u}-\mathbf{B}$ plane at infinity would be the influence of the solar magnetic field, which, however, is apparently too weak to cause a systematic asymmetry of noticeable magnitude, in contrast to what has recently been claimed by Opher et al. (2015). Therefore, the perpendicular displacement m_{\perp} has not been considered further after fitting was completed.

3.2. Cross-sectional Variations

Since the distortion flow is to be incompressible, the constancy of the product $a(z)b(z)$ is a necessary criterion for the consistency of the method in its most basic form as presented in Section 2.1. It is therefore interesting to see to what degree the cross sections of our fitting ellipses can be considered constant. Fig. 6 shows the effective cross-sectional radius $R_j := \sqrt{a_j b_j}$ for the 0.3 nT case. The latter apparently increases toward a maximum at $z \approx -500$ AU and then decreases noticeably toward the far tail. This behavior may at least partly be attributed

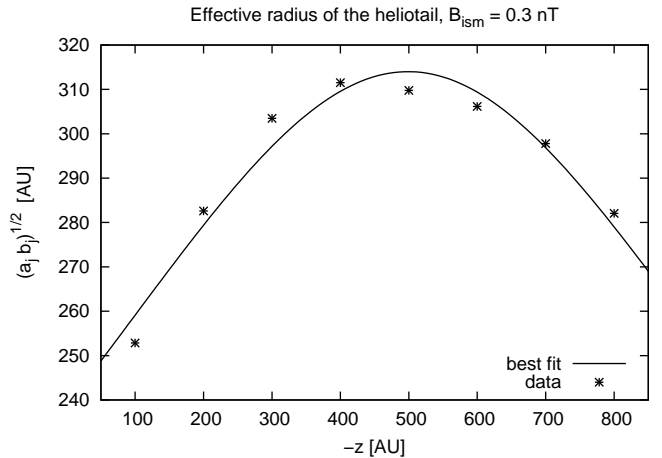


Figure 6. Variation in the heliotail’s effective cross-sectional radius for the 0.3 nT case vs. fitting function (41).

to the fact that the exact heliopause location is somewhat smeared in the simulations, especially in the distant tail, but also to variations of u_z and/or density along z , which are not captured in the simpler form of this approach of constant ab . Therefore, we proceed to apply the more general deformation as outlined in Section 2.4, thereby relaxing the requirement of cross-sectional constancy.

To this end, we first note that according to Fig. 6, the effective radius for the parameter range in question may be reasonably approximated by the heuristic function

$$R_{\text{fit}}(z) := R_c \left[1 + \left(\frac{z - z_c}{\delta_c} \right)^2 \right]^{-1/2} \quad (41)$$

with best-fit parameters $(R_c, z_c, \delta_c) = (314, -499, 583)$ AU. This varying radius is obviously related to the dimensionless squeezing functions $a(z)$ and $b(z)$ via

$$r_{\text{fit}}(z) := \frac{R_{\text{fit}}(z)}{R_{\text{fit}}(0)} = \sqrt{a(z)b(z)}. \quad (42)$$

As can be seen from Fig. 4, the cross sections can be extrapolated to an approximately circular shape at the reference height $z = 0$, in agreement with $a(0) = b(0) = 1$. This also means that it is indeed consistent to place the Sun in the $z = 0$ plane. From Eq. (34), we thus get

$$[R_{\text{fit}}(0)]^2 z_0 = \int_0^z [R_{\text{fit}}(\tilde{z})]^2 d\tilde{z} \quad (43)$$

and hence

$$\frac{z_0}{1 + (z_c/\delta_c)^2} = \delta_c \arctan \left(\frac{\tilde{z} - z_c}{\delta_c} \right) \Big|_0^z \quad (44)$$

$$\Leftrightarrow z_0 = C_1 \left[\arctan \left(\frac{z - z_c}{\delta_c} \right) + C_0 \right] \quad (45)$$

with constants

$$C_0 := \arctan(z_c/\delta_c) \quad (46)$$

$$C_1 := \delta_c + z_c^2/\delta_c \quad (47)$$

which in this particular case evaluate to $C_0 = 0.707$ and $C_1 = 1,010$ AU. If need be, this can immediately be inverted, yielding the explicit form of $z = K(z_0)$ as

$$z = z_c + \delta_c \tan \left(\frac{z_0}{C_1} - C_0 \right). \quad (48)$$

The two squeezing functions then become

$$a(z) = \sqrt{(ab)\frac{a}{b}} = r_{\text{fit}}(z) \sqrt{\eta_{\text{fit}}(0.3 \text{ nT}, z)} \quad (49)$$

$$b(z) = \sqrt{(ab)\frac{b}{a}} = r_{\text{fit}}(z) \frac{1}{\sqrt{\eta_{\text{fit}}(0.3 \text{ nT}, z)}} \quad (50)$$

such that all of the required information is available to turn any (heliospheric or other) magnetic field model with circularly constant cross sections into a more realistic version of itself by adjusting both the aspect ratio and the absolute cross-sectional area to a desired profile.

3.3. Application to the Local ISMF

As an illustrative application, we choose the recent analytical \mathbf{B} field model of the outer heliosheath by R oken et al. (2015), which provides the exact ISMF solution to the stationary induction equation (2) for the case that the flow \mathbf{u} derives from the Rankine half-body potential $\Phi = u_0(q/r + z)$ via $\mathbf{u} = -\nabla\Phi$. Here, u_0 and $4\pi u_0 q$, respectively, denote the LISM flow velocity at infinity and the SW source strength, and $r := \sqrt{x^2 + y^2 + z^2}$ is the Sun-centered radial distance. The quantity \sqrt{q} may be interpreted as the upstream stand-off distance to the stagnation point, such that $q = (125 \text{ AU})^2$ may be considered a reasonable choice for the solar case. The solution shows the expected behavior of the magnetic field piling up in front of and draping around the heliopause, which is easily identified as the surface satisfying

$$H(\mathbf{r}) := 2q - (x^2 + y^2) - z\sqrt{4q - (x^2 + y^2)} = 0. \quad (51)$$

This model thus fulfills the criteria of (i) inclusion of both \mathbf{B} and \mathbf{u} fields which (ii) satisfy Eqs. (1) and (2), and (iii) feature a heliopause with circular cross section, and may therefore be subjected to the procedure outlined in the previous subsection. The distorted field \mathbf{B} at position \mathbf{r} is thus obtained by the following sequence of steps.

1. Find the corresponding position \mathbf{r}_0 in undistorted space via Eqs. (33) and (48), in which $a(z)$, $b(z)$, and $m(z)$ are fixed using Eqs. (49)–(50) and (39)–(40). Since the upwind half-space $z \geq 0$ is taken to be undistorted (implying $\eta(z)|_{z \geq 0} = 1$), the distorting transformation has to be limited to the tail region, i.e. the downwind half-space. Moreover, since the transformation formula (37) involves spatial gradients in $a(z)$ and $b(z)$ that would then lead to discontinuous B field components at $z = 0$, we introduce a spatial averaging function

$$f_{\text{avg}}(z) := \frac{1}{2} \left[1 + \tanh \left(\frac{z}{80 \text{ AU}} \right) \right] \quad (52)$$

and replace all four functions $\mu(z) \in \{a(z), b(z), m(z), F(z)\}$ by

$$\tilde{\mu}(z) := \mu(z) [1 - f_{\text{avg}}(z)] + \mu_0 f_{\text{avg}}(z), \quad (53)$$

thereby allowing them to tend smoothly to their undisturbed values $(a_0, b_0, m_0, F_0) = (1, 1, 0, z_0)$, and ensuring that the distorted fields remain continuous (and even differentiable) due to the now finite derivatives in transformation (37).

2. The undistorted components of \mathbf{B}_0 are evaluated at this position, in this case using Eqs. (57)–(59) of R oken et al. (2015).
3. The distorted components are computed from the undistorted ones using Eq. (37) in conjunction with the above parameters. Remember that while $m'(z) = 0$ according to Eq. (40), the required derivatives $a'(z)$ and $b'(z)$ attain a more complicated form, which, however, may be obtained straightforwardly from their definitions.

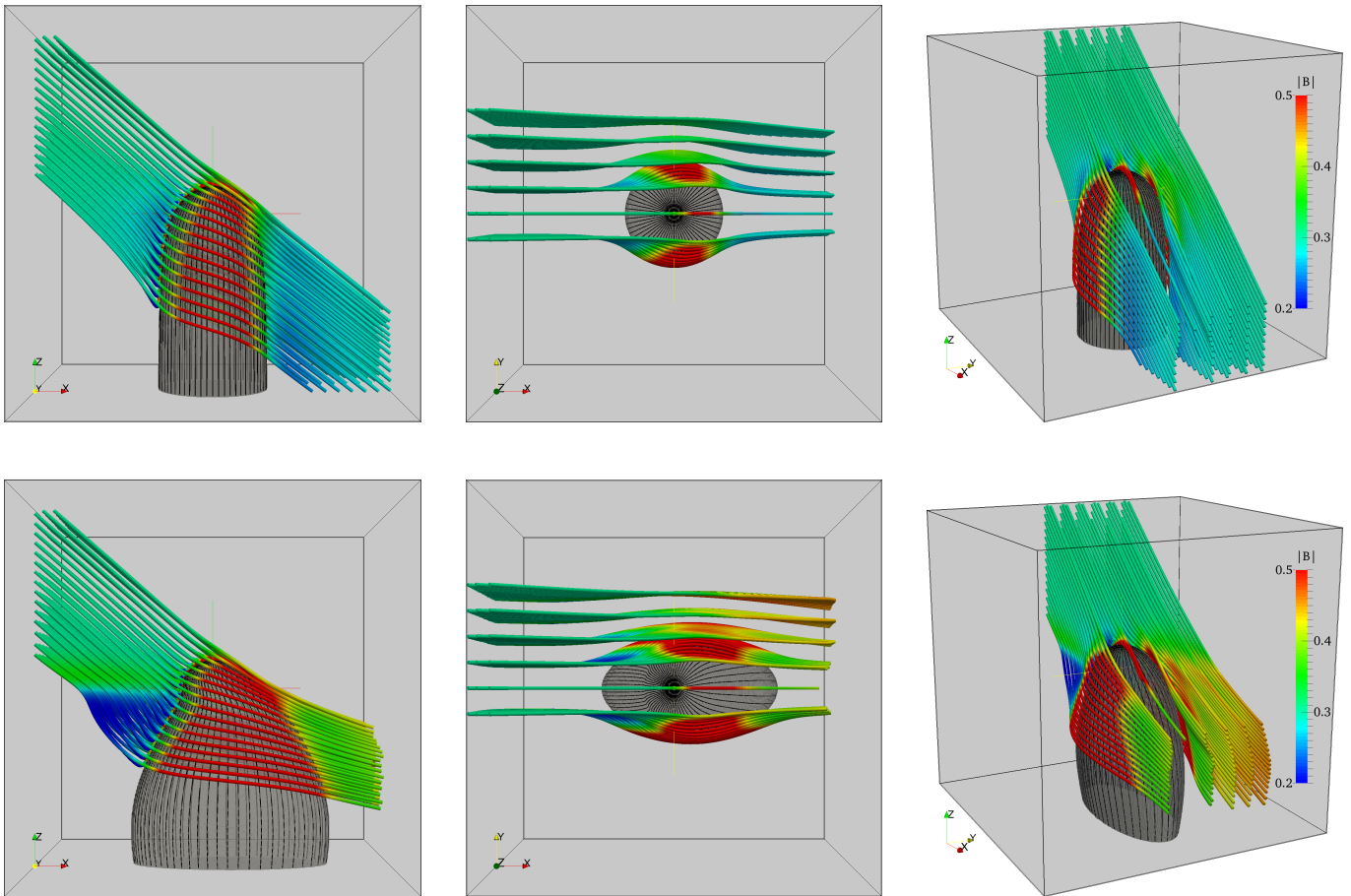


Figure 7. Top row: perspective rendering of selected $\mathbf{B}_0(\mathbf{r}_0)$ field lines of the outer heliosheath model by Røken et al. (2015) for $B_{\text{ism}} = 0.3$ nT, as seen from three different vantage points. The gray surface is the heliopause as defined via $H(\mathbf{r}_0) = 0$ according to Eq. (51), to which the magnetic field is tangential. The black lines on the heliopause are streamlines emanating from the stagnation point. Bottom row: the same situation for $\mathbf{B}(\mathbf{r})$ and $H(\mathbf{r}) = 0$, i.e. after the distortion has been applied to both the magnetic field and the heliopause surface. Note that despite the massive change in shape, the magnetic field remains tangential to the heliopause. $\|\mathbf{B}\|$ values above 0.5 nT are capped.

The resulting configuration can be seen in the side-by-side comparison of Fig. 7. Evidently, the topological properties of the field have been maintained, while the shape of the heliopause has been deformed considerably.

3.4. On the Possibility for Further Extensions

In the deformations employed so far, the squeezing functions a and b have been allowed to vary in z but not within a given x - y plane. Therefore, by construction, they cannot accommodate asymmetric cross-sectional shapes which are found, e.g. in some of the simulation runs presented by Wood et al. (2014). The method of distortion flows can, however, be easily generalized to such cases. To demonstrate this potential, we introduce a second parameter $\beta > 0$ and consider the distortion flow field (3) to be replaced by the slightly more complicated field

$$\mathbf{w}_1 : \begin{pmatrix} x \\ y \end{pmatrix} \mapsto \alpha \left[\begin{pmatrix} x \\ -y \end{pmatrix} + \beta \begin{pmatrix} x^2 \\ -2xy \end{pmatrix} \right] \quad (54)$$

mapping $\mathbb{R}^2 \rightarrow \mathbb{R}^2$, in which the y component of the β term introduces a deformation that varies linearly in x (changing sign at the former symmetry plane $x = 0$), and the x component of that term is chosen such that $\nabla \cdot \mathbf{w}_1 = 0$ is satisfied. The corresponding, now coupled set of equations of motion $\dot{\mathbf{r}}(t) = \mathbf{w}_1[\mathbf{r}(t)]$ has the analytical solution

$$x(t) = x_0 [(x_0\beta + 1) \exp(-\alpha t) - x_0\beta]^{-1} \quad (55)$$

$$y(t) = y_0 \exp(-\alpha t) [x_0\beta [\exp(\alpha t) - 1] - 1]^2. \quad (56)$$

Evaluating these expressions at $t = t_1$, and defining a new constant

$$c := (1/b - 1)\beta \quad (57)$$

with $b = \exp(-\alpha t_1)$ as before, we obtain the transformation

$$x = (x_0/b)(1 - cx_0)^{-1} \quad (58)$$

$$y = (y_0/b)(1 - cx_0)^2, \quad (59)$$

from which the geometric properties of the distorted contour may be easily derived.

Note, in particular, that while b may still be interpreted as the contour’s absolute extension along the y axis in both directions, the position of maximum extension is shifted away from $(x, y) = (0, \pm b)$ toward positive x , while in the perpendicular direction, the contour extends to $([(c \pm 1) b]^{-1}, 0)$ rather than $(\pm b^{-1}, 0)$. This also implies that a spatially bounded and simply connected contour requires $c < 1$. Hence, b continues to adjust the scaling $\propto (1/b, b)$, while the parameter c controls the degree of deformation, ranging from the usual ellipse ($c = 0$) to something like a rounded triangle for values near unity.

After some algebra, the resulting vector transformation turns out to be

$$P_x = \frac{(1 + bcx)^2}{b} P_{0x} + \frac{(b^2 c' x - b') x}{b} P_{0z} \quad (60)$$

$$P_y = 2c(1 + bcx)y P_{0x} + \frac{(1 + 2bcx)b}{(1 + bcx)^2} P_{0y} \quad (61)$$

$$P_z = P_{0z} + [1 + (bc + b'c + 2bc')x]y P_{0z} \quad (62)$$

since $z = z_0$ when embedding the 2D flow field (54) into 3D space. The proof of explicit compliance with constraints (1) and (2) may be carried out in close analogy to the one presented in Appendix A, and is not given here. Fig. 8 illustrates how the parameters b and c may be used to approximate an asymmetric heliopause.

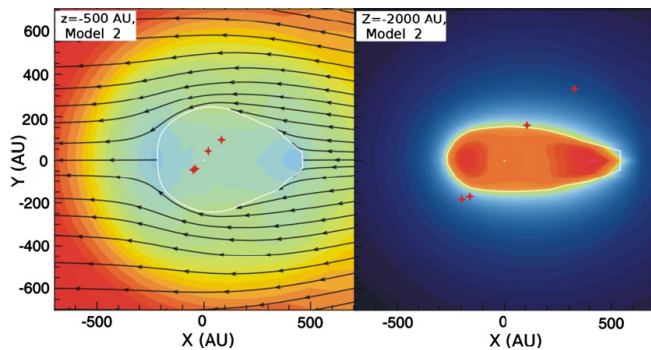


Figure 8. Upper panel: cross-sectional shapes of the heliopause at $z = -500$ AU (left) and $z = -2000$ AU (right), as seen in the simulations by Wood et al. (2014), adapted from Fig. 5 of that work. Lower panel: two distorted contours (blue) as approximations to the simulated cross sections, plotted relative to the reference circle corresponding to $b = 1$ and $c = 0$ (red), which has the same total area due to $\nabla \cdot \mathbf{w}_1 = 0$. The respective parameters employed for the left and right contour are $(b = 0.85, c = 0.10)$ and $(b = 0.60, c = 0.15)$.

4. SUMMARY AND CONCLUSIONS

We have introduced and described the mathematical procedure of distortion flows, by which any pair of 3D magnetic and velocity fields \mathbf{B} and \mathbf{u} can be deformed into different geometric shapes — but with the same topological properties — that are more desirable in a given application. It was proven rigorously that the method conserves both $\nabla \times (\mathbf{u} \times \mathbf{B}) = \mathbf{0}$ and $\nabla \cdot \mathbf{B} = 0$.

For our principal application, namely, the heliospheric tail, we employed sophisticated global simulations to derive heuristic profiles for the former’s cross-sectional aspect ratio and deflection as functions of position along the tail axis, and used this information to deform a recent analytic tail model into a still analytic, yet more realistic version of itself using the distortion flow method.

It should, however, be kept in mind that vector equations different from Eqs. (1) and (2) are not guaranteed to remain unaffected by the squeezing transformation. For instance, the Schwadron et al. (2014) heliosphere model is built around the requirement that there be no currents outside the heliopause ($\nabla \times \mathbf{B} = \mathbf{0}$), and while our approach could certainly be used to deform their magnetic field, the resulting \mathbf{B} field will most likely have $\nabla \times \mathbf{B} \neq \mathbf{0}$.

We note that the use of a (solenoidal) distortion flow does not imply any constraints on the solenoidality (or lack thereof) of the physical fields that are being distorted. In particular, we do not in any way argue for the plasma to be incompressible.

Furthermore, we would like to stress that the applicability of the distortion flow approach outlined in this paper is suitable for any source magnetic field, and does not depend on its particular physical context. Therefore, it is a rather generic tool that could clearly be applied outside the heliospheric context as well. In view of the rather small number of known analytic solutions to the MHD induction equation, the method clearly has the potential to yield the solutions for the magnetized flow around complex geometries simply by starting from a known solution of simpler geometry (like a sphere, see, e.g. the appendix of Isenberg et al. (2015) and references therein) and then deforming this solution as desired.

ACKNOWLEDGMENTS

We are grateful to Gunnar Hornig, Yuri Litvinenko, Frederic Effenberger, and Andreas Kopp for helpful discussions. We acknowledge financial support via the project FI 706/15-1 funded by the Deutsche Forschungsgemeinschaft (DFG). J.H. acknowledges support from NASA grants NNX12AB30G, NNX14AF43G, NNX14AF43G, NSF grant OCI-1144120, and Department of Energy grant SC0008334. We also appreciate discussions at the workshop “Reconnection, Turbulence, and Particles in the Heliosphere” in Queenstown, New Zealand, as well as at the team meeting “Heliosheath Processes and Structure of the Heliopause: Modeling Energetic Particles, Cosmic Rays, and Magnetic Fields” supported by the International Space Science Institute (ISSI) in Bern, Switzerland.

APPENDIX

A. INVARIANCE OF SOLENOIDALITY AND FROZEN-IN CONDITIONS

We proceed to prove that if the vector fields \mathbf{u} and \mathbf{B} are computed using transformation (37) from fields \mathbf{u}_0 and \mathbf{B}_0 satisfying $\nabla_0 \cdot \mathbf{B}_0 = 0$ and $\nabla_0 \times (\mathbf{u}_0 \times \mathbf{B}_0) = \mathbf{0}$, these two equations in deformed coordinates will also hold for \mathbf{u} and \mathbf{B} . To this end, we first need to see how the differential operator $\nabla = (\partial_x, \partial_y, \partial_z)$ in distorted space is related to its undistorted counterpart $\nabla_0 = (\partial_{x_0}, \partial_{y_0}, \partial_{z_0})$. From Eqs. (33) and (34), we have

$$\begin{pmatrix} \partial_x \\ \partial_y \\ \partial_z \end{pmatrix} = \begin{pmatrix} 1/a & 0 & 0 \\ 0 & 1/b & 0 \\ -(a'x + m')/a & -(y b')/b & ab \end{pmatrix} \begin{pmatrix} \partial_{x_0} \\ \partial_{y_0} \\ \partial_{z_0} \end{pmatrix}, \quad (\text{A.1})$$

which is found by explicit calculation via

$$\frac{\partial}{\partial x} = \frac{\partial x_0}{\partial x} \frac{\partial}{\partial x_0} + \frac{\partial y_0}{\partial x} \frac{\partial}{\partial y_0} + \frac{\partial z_0}{\partial x} \frac{\partial}{\partial z_0} = \frac{\partial}{\partial x} \left(\frac{x - m(z)}{a(z)} \right) \frac{\partial}{\partial x_0} + 0 + 0 = \frac{1}{a(z)} \frac{\partial}{\partial x_0} \quad (\text{A.2})$$

$$\frac{\partial}{\partial y} = \frac{\partial x_0}{\partial y} \frac{\partial}{\partial x_0} + \frac{\partial y_0}{\partial y} \frac{\partial}{\partial y_0} + \frac{\partial z_0}{\partial y} \frac{\partial}{\partial z_0} = 0 + \frac{\partial}{\partial y} \left(\frac{y}{b(z)} \right) \frac{\partial}{\partial y_0} + 0 = \frac{1}{b(z)} \frac{\partial}{\partial y_0} \quad (\text{A.3})$$

$$\begin{aligned} \frac{\partial}{\partial z} &= \frac{\partial x_0}{\partial z} \frac{\partial}{\partial x_0} + \frac{\partial y_0}{\partial z} \frac{\partial}{\partial y_0} + \frac{\partial z_0}{\partial z} \frac{\partial}{\partial z_0} \\ &= \frac{\partial}{\partial z} \left(\frac{x - m(z)}{a(z)} \right) \frac{\partial}{\partial x_0} + \frac{\partial}{\partial z} \left(\frac{y}{b(z)} \right) \frac{\partial}{\partial y_0} + \frac{\partial F(z)}{\partial z} \frac{\partial}{\partial z_0} \\ &= -\frac{(x - m(z)) a'(z) + m'(z) a(z)}{a^2(z)} \frac{\partial}{\partial x_0} - \frac{y b'(z)}{b^2(z)} \frac{\partial}{\partial y_0} + a(z) b(z) \frac{\partial}{\partial z_0} \\ &= -\frac{x a'(z) + m'(z)}{a(z)} \frac{\partial}{\partial x_0} - \frac{y b'(z)}{b(z)} \frac{\partial}{\partial y_0} + a(z) b(z) \frac{\partial}{\partial z_0}. \end{aligned} \quad (\text{A.4})$$

Then, by means of transformation (37), we obtain

$$\begin{aligned} \nabla \cdot \mathbf{P} &= \frac{\partial P_x}{\partial x} + \frac{\partial P_y}{\partial y} + \frac{\partial P_z}{\partial z} \\ &= \left(\frac{1}{a} \frac{\partial}{\partial x_0} \right) \left(a P_{0x} + \frac{a' x_0 + m'}{ab} P_{0z} \right) + \left(\frac{1}{b} \frac{\partial}{\partial y_0} \right) \left(b P_{0y} + \frac{b' y_0}{ab} P_{0z} \right) \\ &\quad + \left(-\frac{a' x_0 + m'}{a} \frac{\partial}{\partial x_0} - \frac{b' y_0}{b} \frac{\partial}{\partial y_0} + ab \frac{\partial}{\partial z_0} \right) \frac{P_{0z}}{ab} \\ &= \frac{\partial P_{0x}}{\partial x_0} + \frac{1}{ab} \left[\frac{\partial}{\partial x_0} \left(\frac{a' x_0 + m'}{a} P_{0z} \right) + \frac{\partial}{\partial y_0} \left(\frac{b' y_0}{b} P_{0z} \right) \right] + \frac{\partial P_{0y}}{\partial y_0} \\ &\quad - \frac{1}{ab} \left[\left(\frac{a' x_0 + m'}{a} \frac{\partial P_{0z}}{\partial x_0} \right) + \left(\frac{b' y_0}{b} \frac{\partial P_{0z}}{\partial y_0} \right) \right] + \frac{\partial P_{0z}}{\partial z_0} + P_{0z} ab \frac{\partial}{\partial z_0} \left(\frac{1}{ab} \right) \\ &= \nabla_0 \cdot \mathbf{P}_0 + \frac{P_{0z}}{ab} \left[\underbrace{\frac{\partial}{\partial x_0} \left(\frac{a' x_0 + m'}{a} \right)}_{=a'/a} + \underbrace{\frac{\partial}{\partial y_0} \left(\frac{b' y_0}{b} \right)}_{=b'/b} \right] - P_{0z} \left[\frac{1}{a} \frac{\partial a}{\partial z_0} + \frac{1}{b} \frac{\partial b}{\partial z_0} \right], \end{aligned} \quad (\text{A.5})$$

in which the final pair of square brackets cancels the preceding one due to

$$a' = \frac{\partial a(z)}{\partial z} = ab \frac{\partial a}{\partial z_0} \quad (\text{A.6})$$

and similarly for $b' = \partial_z b(z)$. This proves the invariance of the solenoidality condition for \mathbf{P} .

For the induction equation, we start by defining the undistorted electric field $\mathbf{E}_0 := -\mathbf{u}_0 \times \mathbf{B}_0$, such that $\nabla_0 \times \mathbf{E}_0 = \mathbf{0}$

according to Eq. (2), and then evaluate

$$\begin{aligned}
-\mathbf{E} &= \mathbf{u} \times \mathbf{B} \\
&= \begin{pmatrix} a u_{0x} + (a'x_0 + m')/(ab) u_{0z} \\ b u_{0y} + (b'y_0)/(ab) u_{0z} \\ u_{0z}/(ab) \end{pmatrix} \times \begin{pmatrix} a B_{0x} + (a'x_0 + m')/(ab) B_{0z} \\ b B_{0y} + (b'y_0)/(ab) B_{0z} \\ B_{0z}/(ab) \end{pmatrix} \\
&= \begin{pmatrix} (u_{0y}B_{0z} - u_{0z}B_{0y})/a \\ (u_{0z}B_{0x} - u_{0x}B_{0z})/b \\ (u_{0x}B_{0y} - u_{0y}B_{0x})ab - (u_{0y}B_{0z} - u_{0z}B_{0y})(a'x_0 + m')/a - (u_{0z}B_{0x} - u_{0x}B_{0z})b'y_0/b \end{pmatrix} \quad (\text{A.7}) \\
&= - \begin{pmatrix} E_{0x}/a \\ E_{0y}/b \\ E_{0z}ab - E_{0x}(a'x_0 + m')/a - E_{0y}b'y_0/b \end{pmatrix}
\end{aligned}$$

and further

$$\nabla \times \mathbf{E} = \begin{pmatrix} (1/a) \partial_{x_0} \\ (1/b) \partial_{y_0} \\ -(a'x_0 + m')/a \partial_{x_0} - (b'y_0)/b \partial_{y_0} + ab \partial_{z_0} \end{pmatrix} \times \begin{pmatrix} E_{0x}/a \\ E_{0y}/b \\ E_{0z}ab - E_{0x}(a'x_0 + m')/a - E_{0y}b'y_0/b \end{pmatrix}. \quad (\text{A.8})$$

The x component reads

$$\begin{aligned}
(\nabla \times \mathbf{E})_x &= \frac{1}{b} \frac{\partial}{\partial y_0} \left(E_{0z}ab - E_{0x} \frac{a'x_0 + m'}{a} - E_{0y} \frac{b'y_0}{b} \right) - \left(-\frac{a'x_0 + m'}{a} \frac{\partial}{\partial x_0} - \frac{b'y_0}{b} \frac{\partial}{\partial y_0} + ab \frac{\partial}{\partial z_0} \right) \frac{E_{0y}}{b} \\
&= \underbrace{\left(\frac{\partial E_{0z}}{\partial y_0} - \frac{\partial E_{0y}}{\partial z_0} \right)}_{=(\nabla_0 \times \mathbf{E}_0)_x} a + \underbrace{\left(\frac{\partial E_{0y}}{\partial x_0} - \frac{\partial E_{0x}}{\partial y_0} \right)}_{=(\nabla_0 \times \mathbf{E}_0)_z} \frac{a'x_0 + m'}{ab} + \left(\frac{a}{b} \frac{\partial b}{\partial z_0} - \frac{b'}{b^2} \right) E_{0y} = 0, \quad (\text{A.9})
\end{aligned}$$

in which the last term vanishes for the same reason as above. The y component is computed in complete analogy, and vanishes as well. Finally,

$$(\nabla \times \mathbf{E})_z = \frac{1}{a} \frac{\partial}{\partial x_0} \left(\frac{E_{0y}}{b} \right) - \frac{1}{b} \frac{\partial}{\partial y_0} \left(\frac{E_{0x}}{a} \right) = \frac{1}{ab} \underbrace{\left(\frac{\partial E_{0y}}{\partial x_0} - \frac{\partial E_{0x}}{\partial y_0} \right)}_{=(\nabla_0 \times \mathbf{E}_0)_z} = 0, \quad (\text{A.10})$$

which concludes the proof of the invariance of the induction equation under transformation (37).

The above considerations can be extended to more general distortion flow fields \mathbf{w} as follows. Since in this case the transition from \mathbf{P}_0 to \mathbf{P} proceeds via the evolution equation (31), it is convenient for the proof of the invariance of constraint (1) to consider

$$\begin{aligned}
\partial_t(\nabla \cdot \mathbf{P}) &= \nabla \cdot (\partial_t \mathbf{P}) = \nabla \cdot [\nabla \times (\mathbf{w} \times \mathbf{P}) - (\nabla \cdot \mathbf{P})\mathbf{w} + (\nabla \cdot \mathbf{w})\mathbf{P}] \\
&= 0 - [(\nabla \cdot \mathbf{P})(\nabla \cdot \mathbf{w}) + \mathbf{w} \cdot \nabla(\nabla \cdot \mathbf{P})] + [(\nabla \cdot \mathbf{w})(\nabla \cdot \mathbf{P}) + \mathbf{P} \cdot \nabla(\nabla \cdot \mathbf{w})] \\
&= \mathbf{P} \cdot \nabla(\nabla \cdot \mathbf{w}) - \mathbf{w} \cdot \nabla(\nabla \cdot \mathbf{P}). \quad (\text{A.11})
\end{aligned}$$

If $\nabla \cdot \mathbf{w} = 0$, then this is the well-known advection partial differential equation (PDE)

$$(\partial_t + \mathbf{w} \cdot \nabla) f = 0 \quad (\text{A.12})$$

for $f(\mathbf{r}, t) := \nabla \cdot \mathbf{P}$, meaning that f is passively advected (and thus constant) along flow lines of \mathbf{w} . In particular, $f(\mathbf{r}, t) = 0$ is the only solution that satisfies the appropriate initial condition $f(\mathbf{r}, 0) = (\nabla \cdot \mathbf{P})|_{t=0} = 0$ for all \mathbf{r} . This shows explicitly that $\nabla \cdot \mathbf{P}$ continues to vanish as long as $\nabla \cdot \mathbf{w} = 0$. In fact, we see that any \mathbf{w} with constant (not necessarily vanishing) divergence, like for instance $\mathbf{w} \propto \mathbf{r}$, will conserve the solenoidality of \mathbf{P} . This is intuitively plausible, since such a linear scaling corresponds to an isotropic ‘‘magnification’’ of space that leaves all angles between vectors, etc. unchanged.

Regarding the second constraint (2), we first define the vector quantity to be conserved as $\mathbf{C} := \nabla \times (\mathbf{u} \times \mathbf{B})$, for which we need to show that for the initial condition $\mathbf{C}|_{t=0} = \mathbf{0}$,

$$\begin{aligned}
\partial_t \mathbf{C} &= \partial_t(\nabla \times (\mathbf{u} \times \mathbf{B})) = \nabla \times ([\partial_t \mathbf{u}] \times \mathbf{B} + \mathbf{u} \times [\partial_t \mathbf{B}]) \\
&= \nabla \times ((\mathbf{u} \cdot \nabla)\mathbf{w} - (\mathbf{w} \cdot \nabla)\mathbf{u}) \times \mathbf{B} + \mathbf{u} \times [(\mathbf{B} \cdot \nabla)\mathbf{w} - (\mathbf{w} \cdot \nabla)\mathbf{B}]
\end{aligned} \quad (\text{A.13})$$

vanishes at any $t > 0$. Using the identities

$$[(\mathbf{A} \cdot \nabla)\mathbf{B}]_i = A_j \partial_j B_i \quad (\text{A.14})$$

$$[\nabla \times (\mathbf{A} \times \mathbf{B})]_i = \varepsilon_{ijk} \partial_j (\varepsilon_{klm} A_l B_m) = (\delta_{il} \delta_{jm} - \delta_{im} \delta_{jl}) \partial_j (A_l B_m) = \partial_j (A_i B_j - A_j B_i) \quad (\text{A.15})$$

for general vectors $\mathbf{A}, \mathbf{B} \in \mathbb{R}^3$ (with the convention $\varepsilon_{123} = 1$, and summation over double indices is implied), we obtain for the i th component of Eq. (A.13)

$$\begin{aligned}
\partial_t C_i &= \partial_j \left[(u_k \partial_k w_i - w_k \partial_k u_i) B_j - (u_k \partial_k w_j - w_k \partial_k u_j) B_i \right] \\
&\quad + [u_i (B_k \partial_k w_j - w_k \partial_k B_j) - u_j (B_k \partial_k w_i - w_k \partial_k B_i)] \\
&= \partial_j [(u_k B_j - u_j B_k) (\partial_k w_i) + (u_i B_k - u_k B_i) (\partial_k w_j) + \partial_k (u_j B_i - u_i B_j) w_k] \\
&= \underbrace{\partial_j (u_k B_j - u_j B_k)}_{[\nabla \times (\mathbf{u} \times \mathbf{B})]_k} (\partial_k w_i) + \underbrace{(u_k B_j - u_j B_k)}_{=:S} (\partial_{jk} w_i) + \underbrace{\partial_j (u_i B_k - u_k B_i)}_{=:N} (\partial_k w_j) \\
&\quad + (u_i B_k - u_k B_i) \underbrace{(\partial_{jk} w_j)}_{[\nabla(\nabla \cdot \mathbf{w})]_k} + \underbrace{\partial_{jk} (u_j B_i - u_i B_j)}_{-\partial_k [\nabla \times (\mathbf{u} \times \mathbf{B})]_i} w_k + \underbrace{\partial_k (u_j B_i - u_i B_j)}_{-N} (\partial_j w_k),
\end{aligned} \tag{A.16}$$

in which the second term S vanishes due to the symmetry of ∂_{jk} and the summation over both indices. Upon reverting to vector notation, Eq. (A.16) thus simply becomes

$$\partial_t \mathbf{C} = (\mathbf{C} \cdot \nabla) \mathbf{w} - (\mathbf{w} \cdot \nabla) \mathbf{C} \tag{A.17}$$

when evaluated for the special case $\nabla \cdot \mathbf{w} = 0$ that was already found necessary for the invariance of the solenoidality constraint. Since \mathbf{w} does not depend on t , one can easily use Eq. (A.17) to show via mathematical induction that

$$(\partial_t^n \mathbf{C})|_{t=0} = \mathbf{0} \quad \forall n \in \mathbb{N}_0. \tag{A.18}$$

The PDE system (A.17), together with the initial conditions (A.18), states a Cauchy problem. Under the real analyticity assumption on all coefficients of this PDE system, or rather the distortion vector field \mathbf{w} , one can apply the Cauchy-Kovalevskaya theorem for local existence and uniqueness. From this, it follows that there exists a unique local analytic solution of the Cauchy problem, namely, for \mathbf{C} , in the neighborhood of $t = 0$. Consequently, the Taylor series of \mathbf{C} at $t = 0$ with the conditions (A.18) indeed yields the trivial solution

$$\mathbf{C}(t) = \sum_{n=0}^{\infty} \frac{1}{n!} \left. \frac{\partial^n \mathbf{C}}{\partial t^n} \right|_{t=0} t^n = \mathbf{0}, \tag{A.19}$$

proving that if \mathbf{C} is zero initially, it stays zero at all later times. Again, a vanishing gradient of $\nabla \cdot \mathbf{w}$ is sufficient to obtain this result. This is analogous to the usual MHD induction equation for $\partial_t \mathbf{B}$, which evolves a pre-existing magnetic field \mathbf{B} non-linearly but cannot do so without an initial seed field.

We note in passing that it would not be permissible to conclude already from $\mathbf{C}|_{t=0} = \mathbf{0}$ and the fact that the linear equation (A.17) admits the trivial solution $\mathbf{C} = \mathbf{0}$ that \mathbf{C} has to vanish identically, as is sometimes done erroneously in the literature for the usual, time-dependent MHD induction equation (e.g. Subramanian 2000). This can clearly be seen by the simple example of the ordinary linear differential equation $\dot{g}(t) = (2/t)g(t)$, which possesses the general solution $g(t) = g_1 t^2$ that is non-zero for $t > 0$ and any constant $g_1 = g(1) \in \mathbb{R} \setminus \{0\}$, despite the fact that $g(0) = 0 = \dot{g}(0)$.

B. THE CASE OF ARBITRARY VERTICAL DISPLACEMENTS

The PDE for the determination of the new z component of the general coordinate transformation defined by Eq. (33) and $z_0 = z_0(x, y, z)$, satisfying volume conservation, can be obtained by first computing the exterior derivatives of the original coordinates x_0, y_0 , and z_0 , reading

$$\begin{aligned}
dx_0 &= \frac{1}{a} \left[dx - \left(\frac{[x-m]a'}{a} + m' \right) dz \right] \\
dy_0 &= \frac{1}{b} \left[dy - \frac{y b'}{b} dz \right] \\
dz_0 &= \frac{\partial z_0}{\partial x} dx + \frac{\partial z_0}{\partial y} dy + \frac{\partial z_0}{\partial z} dz.
\end{aligned} \tag{B.1}$$

The corresponding volume three-form becomes

$$dx_0 \wedge dy_0 \wedge dz_0 = \frac{1}{ab} \left[\left(\frac{[x-m]a'}{a} + m' \right) \frac{\partial z_0}{\partial x} + \frac{y b'}{b} \frac{\partial z_0}{\partial y} + \frac{\partial z_0}{\partial z} \right] dx \wedge dy \wedge dz, \tag{B.2}$$

in which the symbol \wedge denotes the standard alternating wedge product on the exterior algebra $\Lambda(\mathbb{R}^3)$. Requiring volume conservation, i.e. $dx_0 \wedge dy_0 \wedge dz_0 = dx \wedge dy \wedge dz$, we immediately find from Eq. (B.2) that

$$\left(\frac{[x-m]a'}{a} + m' \right) \frac{\partial z_0}{\partial x} + \frac{y b'}{b} \frac{\partial z_0}{\partial y} + \frac{\partial z_0}{\partial z} = ab. \tag{B.3}$$

This PDE is the defining equation for the general component transformation $z_0 = z_0(x, y, z)$. In the special case $z_0 = z_0(z)$ discussed in Section 2.4, we have $\partial z_0 / \partial x = 0 = \partial z_0 / \partial y$, and thus from (B.3) we obtain

$$\frac{\partial z_0}{\partial z} = a b . \quad (\text{B.4})$$

Integration leads to

$$z_0 = \int_0^z a(\tilde{z}) b(\tilde{z}) d\tilde{z} , \quad (\text{B.5})$$

which is the component transformation used in Eq. (34).

C. ELLIPSE FITTING PROCEDURE

Let

$$\varphi_{i,j} := \arctan \left(\frac{y_i - m_{\perp,j}}{x_i - m_j} \right) \quad (\text{C.1})$$

be the angle between the x axis and the vector which points from the center of \mathcal{E}_j to the contour point $(x_i, y_i)_j \in \mathcal{H}_j$. The respective distances from the center to that point and to the intersection with \mathcal{E}_j in the same direction are then given by

$$r_{\mathcal{H}_j,i} = [(x_i - m_j)^2 + (y_i - m_{\perp,j})^2]^{1/2} \quad (\text{C.2})$$

$$r_{\mathcal{E}_j,i} = \left[\left(\frac{\cos \varphi_{i,j}}{a_j} \right)^2 + \left(\frac{\sin \varphi_{i,j}}{b_j} \right)^2 \right]^{-1/2} . \quad (\text{C.3})$$

Using the identities $\cos^2 \varphi = 1/(1 + \tan^2 \varphi)$ and $\sin^2 \varphi = (\tan^2 \varphi)/(1 + \tan^2 \varphi)$ allows us to write the quantity to be minimized as

$$\begin{aligned} \Delta_j &= \sum_{i=1}^N |(r_{\mathcal{H}_j,i})^2 - (r_{\mathcal{E}_j,i})^2| (\delta\varphi_{i,j}/2) \\ &\propto \sum_{i=1}^N [(x_i - m_j)^2 + (y_i - m_{\perp,j})^2] \times \left| 1 - \left[\left(\frac{x_i - m_j}{a_j} \right)^2 + \left(\frac{y_i - m_{\perp,j}}{b_j} \right)^2 \right]^{-1} \right| . \end{aligned} \quad (\text{C.4})$$

The contour points $(x_i, y_i)_j$ are generated with equidistant distribution of $\arctan(y_i/x_i)_j$. Strictly speaking, Δ_j would need $\delta\varphi_{i,j} := \varphi_{i+1,j} - \varphi_{i,j}$ to be uniform for all i in order to actually be proportional to the total difference area between \mathcal{H}_j and \mathcal{E}_j . However, given that there is in any case some freedom in the details of a chosen fitting method, this discrepancy is certainly small enough to be safely ignored for the present purpose.

REFERENCES

- Abbasi, R., Abdou, Y., Abu-Zayyad, T., et al. 2010, ApJL, 718, L194
Amenomori, M., & Tibet As γ Collaboration. 2010, ASTRA, 6, 49
Banaszkiewicz, M., & Ratkiewicz, R. 1989, AdSpR, 9, 251
Childress, S., & Gilbert, A. D. 1995, Stretch, Twist, Fold: The Fast Dynamo (Berlin: Springer)
Czechowski, A., & Grzedzielski, S. 1998, GeoRL, 25, 1855
Desiati, P., & Lazarian, A. 2013, ApJ, 762, 44
Drake, J. F., Swisdak, M., & Opher, M. 2015, ApJL, 808, L44
Drury, L. O. ., & Aharonian, F. A. 2008, APh, 29, 420
Grigat, M., & Pierre AUGER Collaboration. 2011, ASTRA, 7, 125
Guillian, G., Hosaka, J., Ishihara, K., et al. 2007, PhRvD, 75, 062003
Gurnett, D. A., Kurth, W. S., Burlaga, L. F., & Ness, N. F. 2013, Sci, 341, 1489
Heerikhuisen, J., Florinski, V., & Zank, G. P. 2006, JGRA, 111, 6110
Heerikhuisen, J., & Pogorelov, N. V. 2010, in ASP Conf. Ser., Vol. 429, Numerical Modeling of Space Plasma Flows, Astronom-2009, ed. N. V. Pogorelov, E. Audit, & G. P. Zank, 227
Heerikhuisen, J., Zirnstein, E. J., Funsten, H. O., Pogorelov, N. V., & Zank, G. P. 2014, ApJ, 784, 73
Isenberg, P. A., Forbes, T. G., & Möbius, E. 2015, ApJ, 805, 153
Izmodenov, V. V., & Alexashov, D. B. 2003, Astronomy Letters, 29, 58
Jäger, S., & Fahr, H. J. 1998, SoPh, 178, 193
Karapetyan, G. G. 2010, APh, 33, 146
Lazarian, A., & Desiati, P. 2010, ApJ, 722, 188
Matsuda, T., & Fujimoto, Y. 1993, 5th Int. Symp. on Computational Fluid Dynamics, Jpn. Soc. of Comput. Fluid Dyn., Sendai, 186
McComas, D. J., Dayeh, M. A., Funsten, H. O., Livadiotis, G., & Schwadron, N. A. 2013, ApJ, 771, 77

- McComas, D. J., Allegrini, F., Bzowski, M., et al. 2014, *ApJS*, 213, 20
- Nagashima, K., Fujimoto, K., & Jacklyn, R. M. 1998, *JGR*, 103, 17429
- Opher, M., Drake, J. F., Zieger, B., & Gombosi, T. I. 2015, *ApJL*, 800, L28
- Parker, E. N. 1961, *ApJ*, 134, 20
- Pogorelov, N. V., Borovikov, S. N., Heerikhuisen, J., Kim, T. K., & Zank, G. P. 2014, in *ASP Conf. Ser.*, Vol. 488, 8th Int. Conf. Numerical Modeling of Space Plasma Flows (ASTRONUM 2013), ed. N. V. Pogorelov, E. Audit, & G. P. Zank, 167
- Pogorelov, N. V., Borovikov, S. N., Heerikhuisen, J., & Zhang, M. 2015, *ApJL*, 812, L6
- Pogorelov, N. V., & Matsuda, T. 1998, *J. Geophys. Res.*, 103, 237
- Pogorelov, N. V., Zank, G. P., & Ogino, T. 2006, *ApJ*, 644, 1299
- Ratkiewicz, R., Barnes, A., & Spreiter, J. R. 2000, *JRG*, 105, 25021
- Richardson, J. D., & Burlaga, L. F. 2013, *SSRv*, 176, 217
- Röken, C., Kleimann, J., & Fichtner, H. 2015, *ApJ*, 805, 173
- Schwadron, N. A., Adams, F. C., Christian, E. R., et al. 2014, *Sci*, 343, 988
- Subramanian, K. 2000, in *The Universe*, Vol. 244, *Thoughts on Galactic Magnetism*, ed. N. Dadhich & A. Kembhavi (The Netherlands: Springer), 169
- Washimi, H., Tanaka, T., & Munakata, K. 1999, in *AIP Conf. Ser.* ed. S. R. Habbal et al., Vol. 471 (Melville, NY: AIP), 827
- Whang, Y. C. 2010, *ApJ*, 710, 936
- Wood, B. E., Izmodenov, V. V., Alexashov, D. B., Redfield, S., & Edelman, E. 2014, *ApJ*, 780, 108
- Yu, G. 1974, *ApJ*, 194, 187
- Zhang, M., Zuo, P., & Pogorelov, N. 2014, *ApJ*, 790, 5